Article in Press

Molecular docking and dynamics reveal novel CDK6 inhibitors for targeted glioblastoma therapy

Muhammad Umer Khan, Maha Munir, Hina Manzoor, Ismail Hamad, Tahir Ali Chohan & Badriyah S. Alotaibi

We are providing an unedited version of this manuscript to give early access to its findings. Before final publication, the manuscript will undergo further editing. Please note there may be errors present which affect the content, and all legal disclaimers apply.

If this paper is publishing under a Transparent Peer Review model then Peer Review reports will publish with the final article.

Molecular Docking and Dynamics Reveal Novel CDK6 Inhibitors for Targeted Glioblastoma Therapy

Muhammad Umer Khan*[1], Maha Munir[2], Hina Manzoor[1], Ismail Hamad[3], Tahir Ali Chohan[4], Badriyah S. Alotaibi[5]

[1]Institute of Molecular Biology and Biotechnology, The University of Lahore, Lahore, Pakistan
[2]University of Catanzaro Magna, Magna, Graecia
[3]Department of Clinical Laboratory Sciences, College of Applied Medical Sciences, Jouf University, Sakaka 72388, Saudi Arabia.
[4]Institute of Pharmaceutical Sciences, UVAS, Lahore,54500, Pakistan
[5]Department of Pharmaceutical Sciences, College of Pharmacy, Princess Nourah bint Abdulrahman University, P.O. Box 84428, Riyadh 11671, Saudi Arabia

Corresponding author: Dr. Muhammad Umer Khan, umer.khan685@gmail.com, Muhammad.umer4@mlt.uol.edu.pk

Maha Munir: maha.munir@studenti.unicz.it

Hina Manzoor: hinamanzor15@gmail.com
Ismail Hamad: ihosman@ju.edu.sa

Tahir Ali Chohan: tahir.chohan@uvas.edu.pk

Badriyah S. Alotaibi: bsalotaibi@pnu.edu.sa

Abstract

Glioblastoma multiform (GBM) is the most deadly type of primary CNS tumor and is linked to dysregulation of the CDK4/6 pathway, poor prognosis, and high rate of post-surgical recurrence. One practical strategy for overcoming treatment resistance in GBM is targeting CDK6. The main goal of this study was to identify new primary amine-containing compounds with specific inhibitory potential against CDK6 using in silico tools. A thorough in silico pipeline comprising ligand-based virtual screening (LBVS), molecular docking, ADMET, Density Functional Theory (DFT) analysis, and molecular dynamics (MD) simulation was used in this investigation. First, molecular docking against CDK6 was performed on 109 bioactive compounds that had been screened using ligand-based virtual screening (LBVS). According to the docking analysis, 48 compounds exhibited more favorable Glide docking scores than the reference compound CCL (-11.174 kcal·mol^{-1}), among which compound 21 showed the most favorable score (-12.811 kcal·mol^{-1}). Additionally, the interaction study demonstrated that the target selectivity of compound 21 was improved by preferential interactions to the polar residues Lys43 and His100. Compound 21 satisfied Lipinski's rule of five (LRo5) and exhibited a favorable predicted toxicity profile, along with predicted blood–brain barrier (BBB) permeability, based on analysis using the SwissADME online tool. Through the demonstration of the stability, moderate reactivity, and minimal off-target potential of compound 21, Density Functional Theory (DFT) studies provided additional validation for its electrical characteristics. Further molecular dynamics simulation straddling 250ns confirmed the stability and flexibility of compound 21. These findings demonstrated compound 21 as a predicted lead and it could serve as a potential therapeutic agent targeting CDK6 in GBM treatment. However, in vitro and in vivo studies are required for the further clinical application of compound 21.

Keywords: CDK6, Glioblastoma multiforme (GBM), molecular docking, molecular dynamics (MD) simulations, and density functional theory (DFT).

Introduction

Glioblastoma multiforme (GBM) represents the most prevalent form of aggressive brain cancer in adults. It is characterized by abnormal growth and invasiveness, often resulting in a poor prognosis despite extensive treatments [1-3]. Glioblastoma multiforme (GBM) is a highly lethal and fatal form of brain tumor hallmarked by significant molecular heterogeneity and dismal prognosis. It accounts~ 57% of all gliomas and 48% of all primary central nervous system (CNS) malignancies [5]. It most commonly affects individuals around the age of 65, with the highest incidence in those aged 75–84, and is more frequent in males [2,6]. Only a small percentage of patients survive beyond three years, and overall treatment progress has been minimal over recent decades [7,8].

The genomic instability in GBM primarily involves the aberration in the cell cycle, particularly involving G1 and S1 phases, as well as G2/M checkpoint phase [9]. Cyclin-dependent kinases (CDKs) are essential cellular checkpoints. In a homeostatic environment, the G1 phase is responsible for DNA synthesis, triggered by the activation of CDK4 and CDK6. Additionally, the checkpoint transition from S phase to G2/M phase is mainly driven by cyclin A2 via CDK2. At the final stage of interphase, mitosis occurs, which is aided by the activation of CDK1 [10]. A detailed genomic profile of GBM has been stratified

into various molecular subtypes, as well as reported recurrent alterations in key regulatory cascades related to CDKs, encompassing CDKN2A/B deletions, TP53 and PTEN mutations, EGRF, CDK4, and CDK6 amplifications [11,12]. Notably, dysregulation in the CDK4/6-Retinoblastoma (CDK4/6-Rb) axis accounts for~ 80% of GBM cases [13]. Owing to the high frequency of changes in the CDK4/6 pathway, several CDK4/6 specific inhibitors, such as ribociclib, palbociclib, and abemaciclib, have been developed [15]. The U.S. The Food and Drug Administration (FDA) has approved these inhibitors for the treatment of breast cancer molecular subtypes, which is exciting [20]. It has been discovered that the CDK4/6 pathway is crucial in GBM. In particular, it has been demonstrated that CDK4 overexpression increases the growth of GBM tumors and lowers patient survival [21]. By encouraging resistance to cell cycle arrest, apoptosis, and radiation, CDK4/6 has also been demonstrated to support the mesenchymal subtype of GBM, which is a more aggressive phenotype [22-24]. While several clinical trials have revealed limited efficacy for CDK4/6 [19,25], several in vitro and in vivo experiments have shown encouraging results for CDK4/6 [23,26]. This disparity between preclinical data and clinical trial results clearly indicates CDK4/6 resistance as a possible mechanism underlying the limited efficacy. Consequently, blocking CDK4/6 may be a useful therapeutic approach for GBM.

Glioma cells have an advantage due to the nature of the blood-brain barrier (BBB), suppressive tumor microenvironment, and tumor heterogeneity. Consequently, chemotherapeutics, targeted treatments, and immunotherapy are less effective [7,27]. The CNS is an immune-privileged site with limited access that influences T cell activity because of characteristics such as the BBB, antigen-presenting cell (APC) scarcity, lymphatic channels, low Major Histocompatibility Complex (MHC) class II expression, and transforming growth factor (TGF)-ß expression [28,29]. Radiation and chemotherapy are the next steps in the usual treatment plan for GBM, which includes safe surgical resection of the tumor [30,31].

Despite receiving numerous treatments, patients with GBM frequently have poor prognoses. Temozolomide (TMZ) is the first-line chemotherapeutic agent, especially when combined with alkylating medication TMZ [32,33]; however, systemic toxicity has been noted [29]. This emphasizes the necessity of developing novel treatment approaches for patients with GBM [33,34]. These conventional treatments may initially be effective in eliminating tumors; however, they are also associated with a significant risk of cancer spread and recurrence due to factors such as surgical stress, high expenses, ineffective medications [28,35] and cytotoxicity in healthy tissues [36]. Thus, identifying new therapeutic targets and strategies is crucial for improving the prognosis and quality of life of patients with cancer.

The FDA has approved several CDK inhibitors for the treatment of different advanced-stage metastatic malignancies [16,37]. However, no CDK inhibitors are currently licensed for GBM treatment. Recent research has shown that using an oncolytic virus in conjunction with CDK4/6 inhibitor therapy inhibits the growth of GBM tumors, increasing the survival rate in mouse models [38]. According to the research, CDK4/6 targeting may have inhibitory efficacy in GBM, and such strategies are crucial for improving the prognosis and quality of life of cancer patients.

Based on the above prospectus, the recent study was focused on identifying novel small molecular inhibitors targeting CDK6 in managing GBM therapeutics. The current study was focused on applying *in silico*-based computational tools such as ligand-based virtual screening (LBVS) for the retrieval of novel compounds. Molecular docking studies were also carried out to investigate the inhibitory potential of novel compounds, which were further validated by performing molecular dynamics (MD) simulations. Moreover, the pharmacological and toxicity profile of the small molecules was also evaluated to screen out the lead compound with favorable drug-like characteristics, further supported by density functional theory (DFT) studies to determine the electronic and molecular reactivity of the compound.
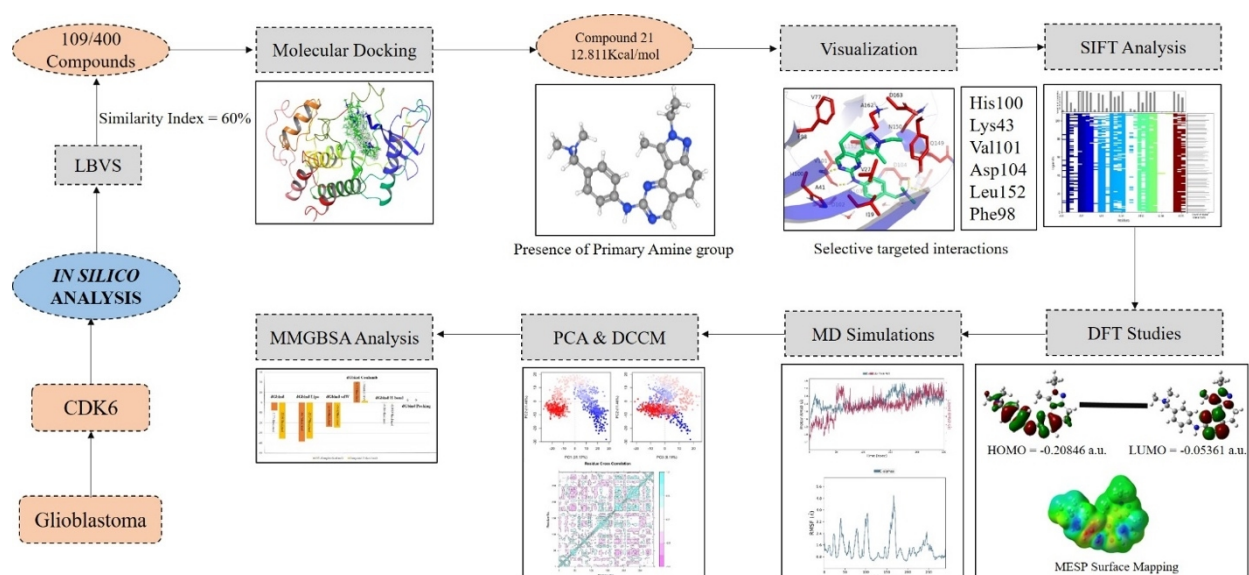
Figure 1: A comprehensive workflow for the current study

Methodology

Retrieval of Target Protein

The structure of the target receptor CDK6 (PDB ID: 6OQO) was retrieved from the Protein Data Bank (PDB) at a resolution of 1.98Å and downloaded in PDB format. The crystal structure of CDK6 (PDB ID: 6OQO) was classified under the transferase family of *Homo sapiens* and consisted of a chain length of 291 residues. The crystal structure was also devoid of any mutation. Additionally, a native co-crystal ligand (CCL), PubChem CID: 138911331, was also associated with the alpha chain of the target receptor [39] (Figure 1).

Ligand-Based Virtual Screening (LBVS)

The CCL (PubChem CID: 138911331) residing within the target protein CDK6 (PDB ID: 6OQO) was taken as the reference ligand for LBVS to identify the molecular similarities. For drug discovery, the string of canonical SMILES of CCL was entered as the query molecule. Swiss Similarity was run in a single cycle by selecting the Chembl drug-like library using a combined 2D and 3D approach. The top compounds generated through this library were used for further *in silico* analysis.

Retrieval of Ligands

The resulting LBVS compounds and the CCL were obtained from the PubChem database. These compounds were then saved in SDF format for molecular docking purposes and MOL format for DFT studies.

Assessment of Chemical Diversity

To assess the chemical diversity of the screened compounds, a ChemMine tool, a web server based on cheminformatics, was used. This tool supported a wide range of functionalities, including cluster analysis. The SMILES of the compounds were uploaded to the workbench and analyzed for clustering [40].

Preparation of Ligands

All SDF formatted compounds were then subjected to the LigPrep tool of Schrodinger 2020-3v12.5 for their preparation. Initially, all compounds were protonated and ionized using the Epik module at an optimum pH of 7.0±2, followed by desalting and generating tautomers. Furthermore, 32 poses for each ligand were generated by retaining specific chiralities, followed by minimization by applying a force field of OPLS3e [41].

Preparation of Target Proteins

The target protein used in the current study, CDK6 (PDB ID: 6OQO), was prepared using the Protein Preparation Wizard tool in PDB format. Firstly, in the preprocessing stage, Prime job was performed to identify and fill the structural gaps due to absent loops and side chains. Thereafter, the Epik module generated the tautomeric states of heteroatoms at an optimal pH of 7.0 ± 2. Secondly, the PROPKA module was chosen for H-bond network optimization at an optimum pH of 7.0, followed by the removal of water molecules within the range of 3Å. Finally, the crystal structure of the protein was minimized under an applied force field of OLPS3e [42]. Additionally, to investigate and analyze the interaction pattern of these novel compounds with the active site residues of the binding cavity, a glide grid was generated

on the energy-minimized protein within the center of the working space of CCL [42,43].

Molecular Docking

To investigate the binding potential of these novel compounds with the target protein, CDK6, docking analysis was performed by subjecting the minimized output files of the compounds and the receptor to the ligand docking tool in Schrödinger 2020-3v12.5. Extra precision mode was selected to accommodate ligand flexibility during the docking protocol. Per-residue interaction scores and root-mean square deviation (RMSD) were calculated for each input ligand conformation. Subsequently, post-docking minimization was conducted, and docking scores were generated for all compound [44]. Finally, the interactions were analyzed on Maestro Schrodinger 2020-3v12.5 through the ligand interaction tool as well as using PyMOL software v3.4.0.

Structural Fingerprinting (SIFT) Analysis

The structural interaction fingerprinting analysis was performed for the top 109 compounds on Schrodinger 2020-3v12.5, to assess the interacting residues of active site at residual level [45]. SIFT analysis provided the critical hotspot residues of the active site of target protein CDK6, that are consistently involved in interaction with the compounds within the docked complexes. This analysis provided a static snapshot, by residual mapping of interactions including backbone interactions, polar residues, hydrophobic residues, and hydrogen bond acceptors and donors. Furthermore, the cluster analysis of top compounds was also performed to classify the ligands based on these interaction fingerprints.

In Silico Pharmacological Analysis

The pharmacological characteristics of all compounds were evaluated using the online web server SwissADME to assess the absorption, distribution, metabolism, and excretion (ADME) properties of the query molecules. This

server employed molecular fingerprinting algorithms to assess the pharmacological features [46]. The string of SMILES representations of the compounds was utilized as input to evaluate the drug-like characteristics.

In Silico TOX Prediction

StopTox, a machine learning approach, was implemented to predict the possible acute toxicity upon instant contact with the respective compound. The *in vivo* assays were employed on the models to assess the toxicity of 6-Pack [47]. The SMILES notations of the compounds were incorporated as input files to predict toxicity.

Density Functional Theory (DFT) Studies

The molecular characteristics of the lead molecule were determined using DFT analysis. The energetically advantageous conformation was obtained using the Gaussian 09 W program after the chemical in the MOL format was imported into the Gauss View software v.5.0.8 interface. The physiological phase of a conductor-like polarizable continuum model (CPCM) was studied using Becke's 3-parameter Lee-Yang-Parr (B3LYP) technique with a basis set of 6-311+G [48]. Using the checkpoint file (. chk*), frontier molecular orbitals (FMOs), and molecular electrostatic potential (MESP) mapping for the molecule were carried out. Gauss View software v.5.0.8 was then used to further visualize the results. Using Koopman's theorem, the global reactivity parameters were computed [49].

Molecular Dynamics (MD) Simulation

MD simulations were conducted for the lead drug and CCL at 250 ns using Desmond, a Schrodinger suite, to gain more insight into the conformational stability of the docked complexes on a dynamic scale. First, the target protein CDK6 was optimized and energy-minimized using the Protein Preparation tool. Steric conflicts and aberrant geometries were eliminated. Subsequently, a system was constructed, and an orthorhombic box was created using the

transferable intermolecular potential 3 points (TIP3P) solvent model and the OPLS_2005 force field. Counter ions were introduced to the system to neutralize it, and 0.15 M NaCl was added to the complex to promote physiological conditions. Furthermore, for the 250 ns simulations, the temperature and pressure were maintained at 300 K and 1atm, respectively. The number of hydrogen bonds, radius of gyration (Rg), root-mean-square deviation (RMSD), and root-mean-square fluctuation (RMSF) were evaluated after all trajectories were saved for examination at 100 ps intervals. The R language script and Bio3D package were used to conduct principal component analysis (PCA) and dynamic cross-correlation matrix (DCCM) investigations, respectively.

Molecular mechanics and generalized born surface area (MM-GBSA) calculations

The Prime module was utilized to evaluate the binding free energy (G_{bind}) for each docked complex through the MM/GBSA approach. To determine G_{bind}, the following equation employed the VSGB solvent model and rotamer conformations, under an applied force field of OPLS_2005. Where, dG_{bind} = binding free energy, $G_{complex}$ = free energy of the complex, $G_{protein}$ = free energy of the target protein, and G_{ligand} = free energy of the ligand.

$$dG_{bind} = G_{complex} - (G_{protein} + G_{ligand})$$

Results

Ligand-Based Virtual Screening

The LBVS resulted in 400 bioactive compounds from the Chembl drug-like library, having a similarity score ranging from 0.872 to 0.343, mentioned in *Supplementary File 1*. The resultant compounds with a similarity index of ≥ 0.600 against the reference compound (PubChem CID: 138911331) were selected for *in silico* docking analysis. The 3D conformations, similarity index,

and SMILES of all resulting 109 compounds are illustrated in *Supplementary Table 1*.

Assessment of Chemical Diversity

Cluster analysis, which evaluates the chemical array of the top-screened compounds and produces important information on their distribution and structural variety, was performed using ChemMine software. Indicating that molecules with comparable structures were clustered according to their chemical fingerprints, the 2D scatter plot displayed several clusters (Supplementary Figure 1). The observed pattern indicated that distinct subgroups of compounds had core scaffolds and pharmacophores. In particular, one compound was a singleton in the center of the plot, highlighting the difference in its chemical structure from the others. Overall, these findings support the idea that the LBVS method increases the possibility of identifying strong and specific CDK6 inhibitors by recovering a chemically varied and non-redundant collection of bioactive molecules with wide structural variety.

Docking Analysis

All 109 compounds, including CCL, underwent molecular docking to examine their possible binding affinities and patterns of interaction with the crucial interacting residues of the active site of the target protein CDK6 (PDB ID: 6OQO). Of the 109 compounds, 48 had docking scores higher than CCL (-11.174 kcal/mol), according to the docking values displayed in Table 1. These findings highlight the strong CDK6 inhibitory capability of these drugs (PDB ID: 6OQO) in the fight against GBM. Additionally, all other compounds also exhibited remarkable docking score but were lower than CCL, as shown in *Supplementary Table 2*. Furthermore, these docking results were validated by re-docking the CCL (PubChem CID: 138911331) within the active site of the target receptor CDK6 (PDB ID: 6OQO). The validity and effectiveness of

the docking methodology were demonstrated by the re-docked superimposed structure, which displayed an RMSD value of less than 2Å (*Supplementary Figure 2*).

Table 1: Docking scores of top-scored compounds retrieved from LBVS, against target protein CDK6 (PDB ID: 6OQO).

Target Protein CDK6 (PDB ID: 6OQO)			
Compounds	**Docking Scores** (Kcal/mol)	**Compounds**	**Docking Scores** (Kcal/mol)
CCL	-11.174	51	-12.026
21	-12.811	72	-11.907
69	-12.776	88	-11.794
34	-12.553	48	-11.791
57	-12.517	98	-11.76
93	-12.509	30	-11.703
54	-12.487	9	-11.696
42	-12.463	107	-11.657
91	-12.385	28	-11.636
59	-12.312	105	-11.631
41	-12.299	17	-11.605
83	-12.264	6	-11.556
44	-12.26	38	-11.545
77	-12.216	31	-11.505
56	-12.196	102	-11.437
103	-12.192	63	-11.43
89	-12.188	20	-11.419
65	-12.173	18	-11.417
64	-12.151	108	-11.403
50	-12.109	52	-11.331
15	-12.1	80	-11.237
100	-12.061	75	-11.214
45	-12.038	23	-11.208
58	-12.035	36	-11.197
62	-12.035		

Visualization and Analysis of Binding Interactions:

Supplementary Figure 3 illustrates the interactions of the 48 highest-scoring chemicals in relation to CCL. Notably, as shown in Figure 2, all drugs occupied the same active site and interacted with amino acid residues that

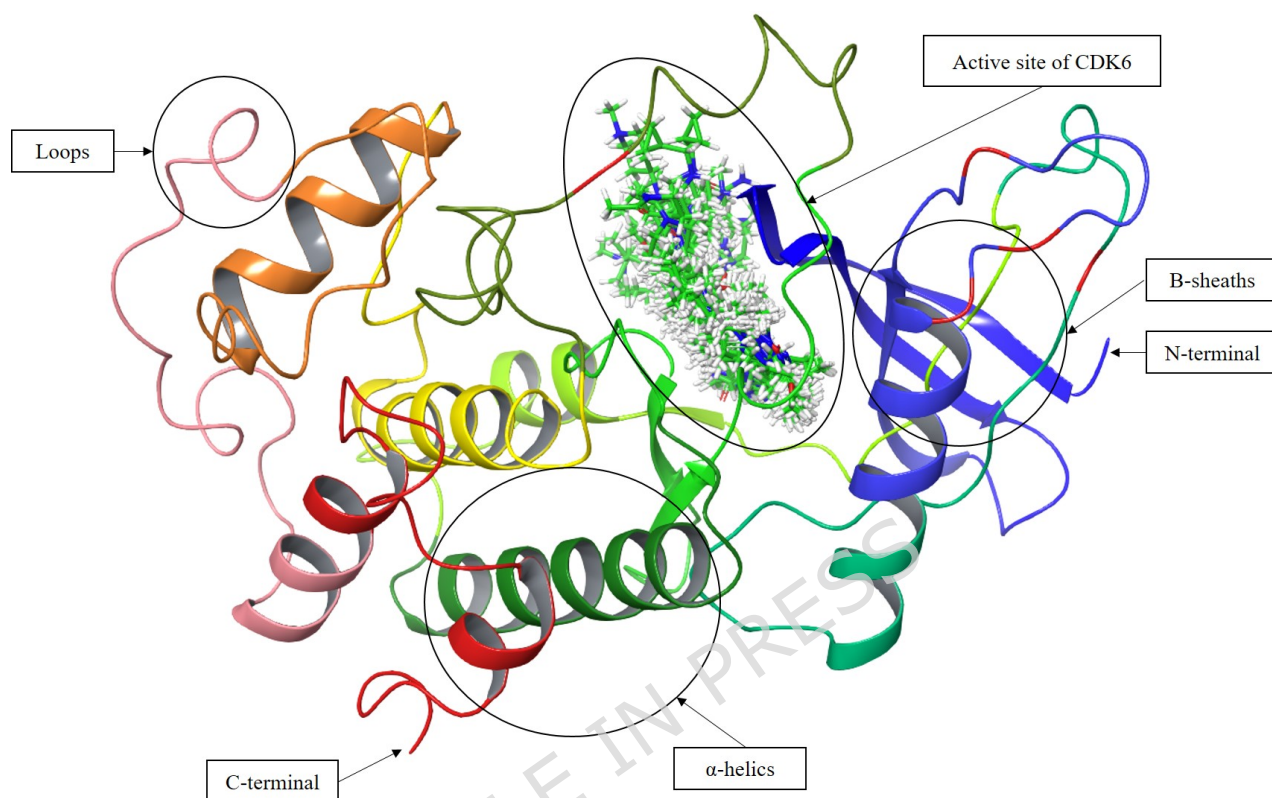are essential for binding stability and specificity when targeting CDK6 (PDB ID: 6OQO) in GBM.

Figure 2: Visualization of the active site of target protein CDK6 (PDB ID: 6OQO).

Important information on the interaction patterns of the top seven drugs is provided by their 2D interactions with the target protein CDK6 (PDB ID: 6OQO). As shown in Figure 3, a typical hydrogen (H) bond with charged and polar residues (Glu99, Asp102, Asp104, and His100) was established according to the CCL interaction pattern, demonstrating the stability and polarity of the docked complex. Additionally, the Asp102 residue helped develop water-mediated connections, demonstrating the adaptability of the docked complex. Furthermore, hydrophobic CDK6 active site residues form non-covalent interactions with CCL, ultimately aiding in the stabilization of the benzene rings of the protein.

Asp102, Asp104, and Glu99 were among the significant interacting residues with which the other compounds established conventional H-bonds. By keeping the compounds at the target receptor CDK6's active area, these negatively charged residues help preserve electrostatic compatibility (PDB ID: 6OQO). The involvement of a polar residue (His100) enabled the formation of an H-bond, which further defined the interactions. However, the positively charged residue Lys43 made vital contact with the triazole ring of each molecule. This type of interaction is crucial for selectively targeting CDK6 protein. Consequently, the development of advantageous contacts or H-bonds indicated the compounds' selectivity and binding affinity within the active site, in addition to helping to stabilize them.

Additionally, the docked complexes were largely stabilized by noncovalent hydrophobic contacts. The hydrophobic pocket is formed by the interaction of several important residues, including Val101, Leu152, Val77, Ala41 and Phe98. Ligand anchoring within the CDK6 protein's active site was maintained by the involvement of these residues in binding interactions. An aromatic residue, phe98, was also observed to form π-π stacking within the aromatic moiety of all observed compounds. Such type of interactions played a significant role in stabilization through electronic cloud contact, suggesting more favorable binding of these compounds with the CDK6 receptor.
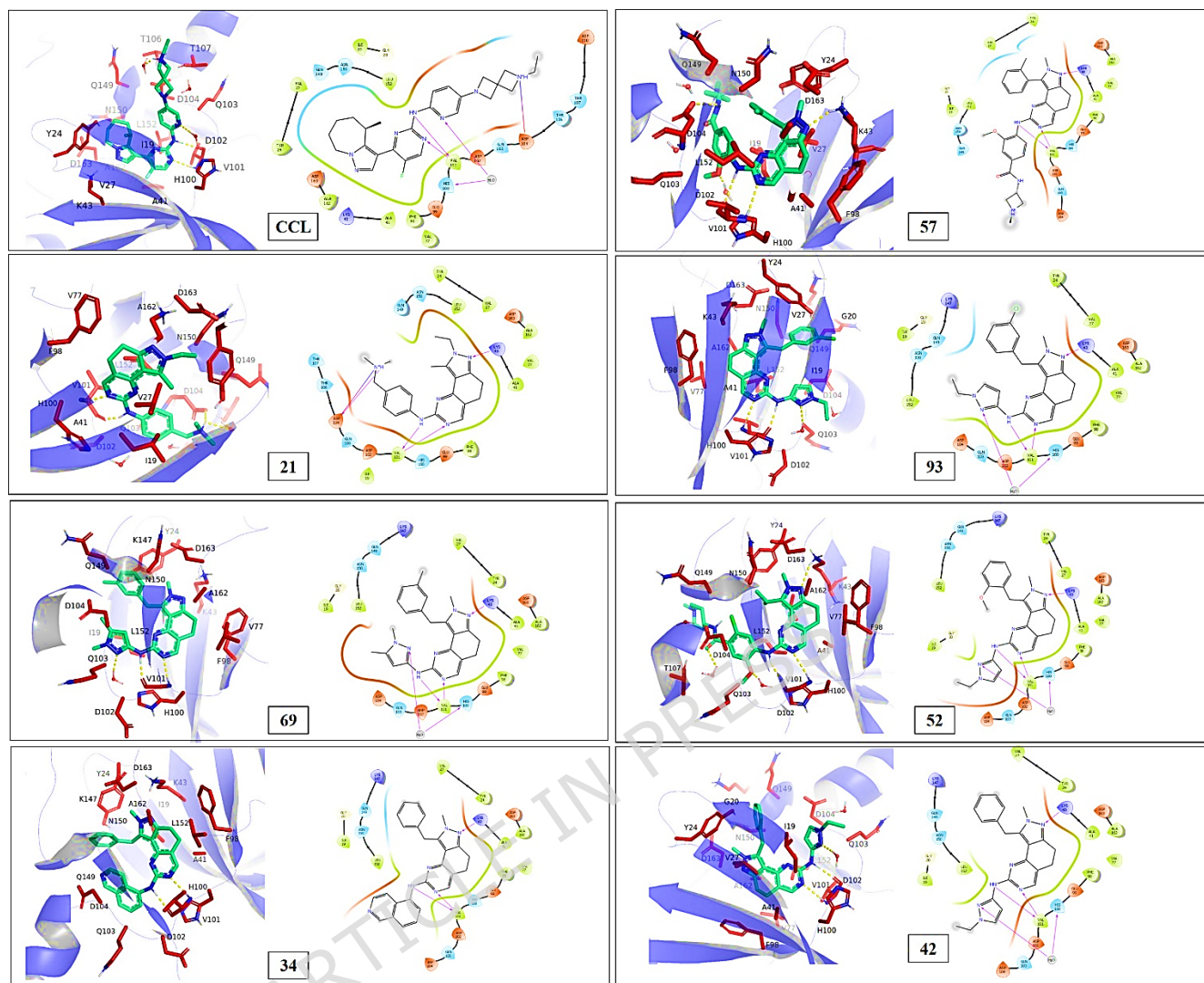
Figure 3: Visual representation of binding interaction pattern of the top seven screened compounds against CDK6 (PDB ID: 6OQO).

Additionally, the interaction analysis of the top seven compounds against the target protein CDK6 demonstrated conserved key residues forming bonds at specified distances, illustrated in Table 2. These residues were consistently involved in forming various types of interactions, including Van der Waals, H-bonds, pi-pi stacking, alkyl, pi-alkyl, carbon-hydrogen bonds, Pi-anion, and Amide-pi stacking, which ultimately contributed to enhancing the stability of the docked complexes.

Table 2: An overview to the types of interactions, key residues, and the bond distances of the CCL and top 7 docked complexes against CDK6 (PDB ID: 6OQO).

Compounds	Chembl IDs	Type of interactions	Key Residues	Bond Distance (Å)
CCL	-	H-Bond	Val101	2.25
		carbon-hydrogen bonds	Asp104	2.78
			Glu99	2.56
			His100	4.51
		pi-pi stacking	Gln103	4.55
		alkyl, pi-alkyl	Val27	5.23
			Ile19	4.41
			Tyr24	5.03
			Ala162	4.37
			Ala41	4.19
			Leu152	4.34
21	CHEMBL3656631	H-Bond	Lys43	5.35
			Val101	4.06
			Asp104	4.36
		carbon-hydrogen bonds	Glu99	2.37
		pi-pi stacking, polar	His100	5.03
		alkyl, pi-alkyl	Phe98	5.42
			Ala41	5.58
			Val77	5.11
			Leu152	5.20
69	CHEMBL3656738	H-Bond,	Lys43	4.87
			Val101	3.93
		carbon-hydrogen bonds	Glu99	2.38
		pi-pi stacking, polar	His100	6.55
			Gln103	4.53
		alkyl, pi-alkyl	Asp104	5.29
			Phe98	4.57
			Ala41	4.98
			Val77	5.05
			Leu152	5.22
34	CHEMBL3652858	H-Bond,	Lys43	4.90
			Val101	3.87
		carbon-hydrogen bonds	Glu99	2.49
		pi-pi stacking,	His100	6.62
			Gln103	5.06
		alkyl, pi-alkyl	Asp104	4.61
			Phe98	4.62

			Ala41	5.07
			Val77	5.10
			Leu152	5.26
57	CHEMBL3660975	H-Bond,	Lys43	4.53
			Val101	4.14
			Asp104	5.01
		carbon-hydrogen bonds	Ile19	2.39
			Glu99	2.69
			Asp102	2.37
		pi-pi stacking	Gln103	4.59
		alkyl, pi-alkyl	Phe98	4.42
			Ala41	6.16
			Val77	5.39
			Leu152	5.11
93	CHEMBL3656707	H-Bond, carbon-hydrogen bonds	Lys43	4.99
			Val101	3.91
			Glu99	2.47
		pi-pi stacking,	Gln103	4.42
		alkyl, pi-alkyl, polar	Asp104	4.63
			Phe98	4.82
			Ala41	5.59
			Val77	5.15
			Leu152	5.16
54	CHEMBL3656712	H-Bond,	Lys43	4.72
			Val101	3.92
		carbon-hydrogen bonds	Glu99	2.53
			Ile19	2.30
		pi-pi stacking,	Gln103	4.40
		alkyl, pi-alkyl, polar	His100	5.27
			Asp104	4.62
			Phe98	4.57
			Ala41	6.12
			Val77	5.09
			Leu152	5.77
42	CHEMBL3656665	H-Bond,	Lys43	4.89
			Val101	3.93
		carbon-hydrogen bonds	Glu99	2.57
		pi-pi stacking, polar	His100	5.56
			Gln103	4.46
		alkyl, pi-alkyl	Asp104	6.02
			Phe98	4.72
			Ala41	6.14
			Val77	5.29

			Leu152	5.14

SIFT Analysis

To gain deeper insight beyond docking scores, SIFt analysis was performed to map ligand–residue interactions at the atomic level. The SIFT analysis further provided a detailed analysis of the binding interactions of all 109 compounds at the residual level between the target protein CDK6 and the compounds, as shown in Figure 4. The analysis revealed that negatively charged residues such as Glu99, Asp102, Asp104, and His100 were mainly involved in the formation of H-bonds with the majority of the compounds. A positively charged residue, Lys43, was also one of the key residues involved in the formation of a favorable H-bond with the heteroaromatic rings of the compounds. Additionally, Val101, Leu152, Val77, Ala41, and Phr98 are majorly dominating in forming non-polar hydrophobic interactions with most of the compounds. Therefore, Glu99, Asp102, Asp104, Lys43, His100, Val101, Leu152, Val77, Ala41, and Phr98 residues could be considered as hotspot residues, which are critical in binding interactions with the small molecule inhibitors for GBM therapeutic management.
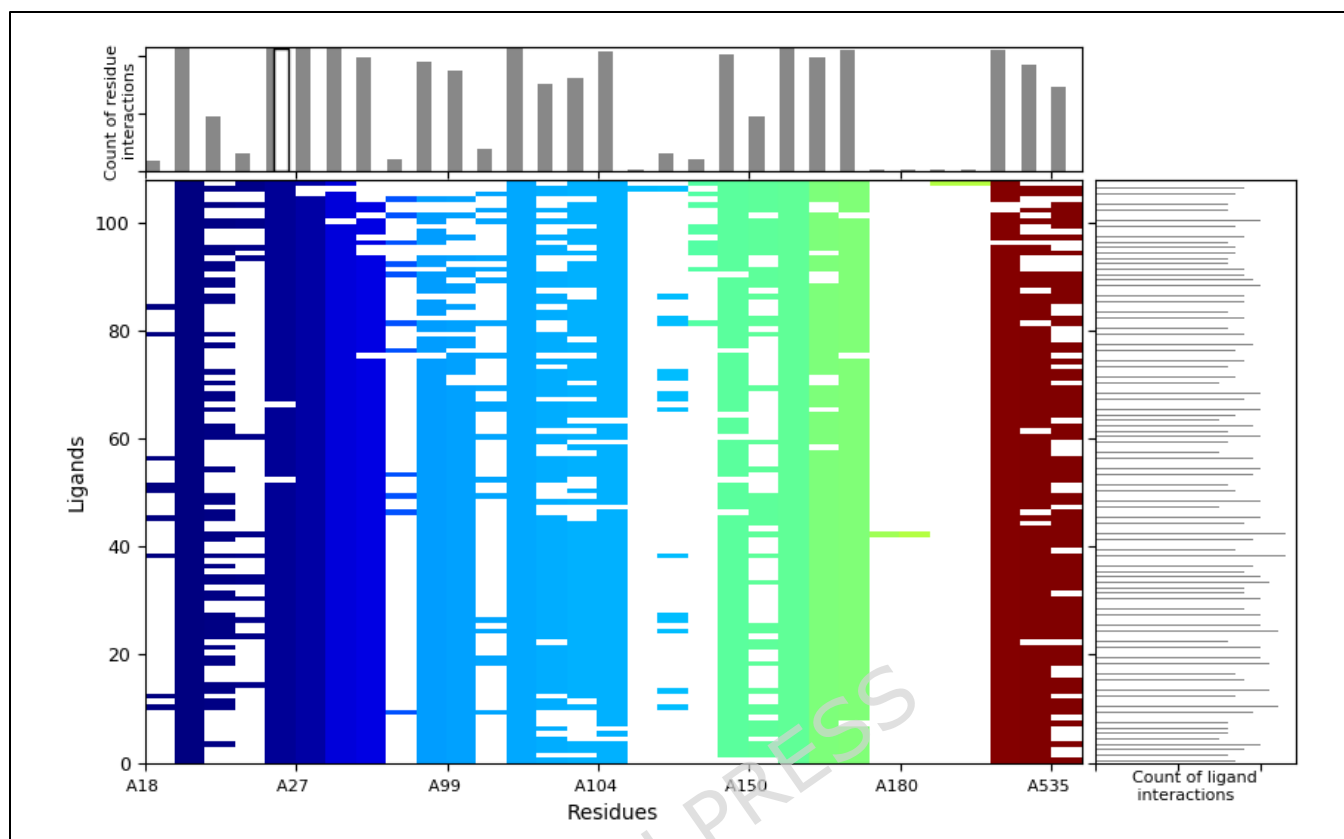
Figure 4: Visual representation of Fingerprinting analysis of all screened compounds with the hotspot residues of target protein CDK6 (PDB ID: 6OQO).

Additionally, structural and interactional diversity was also evaluated through a hierarchical clustering dendrogram by using the interaction fingerprinting tool. The dendrogram shown in Figure 5, clusters 109 top screened complexes based on their interaction fingerprints with the target protein CDK6, highlighting distinct clusters of the compounds with similar interaction profiles, giving an insight into the structural-activity relationship (SAR). It is interesting to note that the compounds that were grouped together had similar pharmacophoric characteristics, as demonstrated by their identical binding patterns in the active region of CDK6. Overall, our interaction-based clustering demonstrated the potential of bioactive medicines as selective CDK6 inhibitors for the treatment of GBM by validating the variety of binding mechanisms among them.
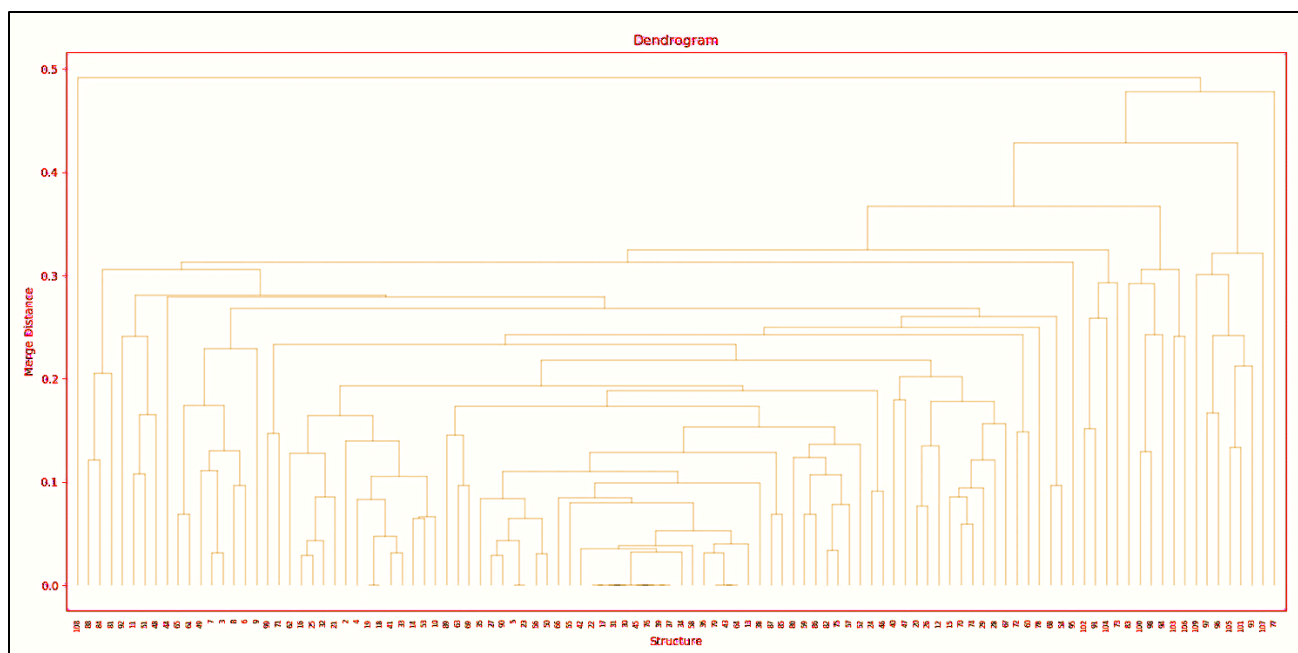
Figure 5: Hierarchical clustering dendrogram of the top 109 screened compounds based on interaction fingerprint similarity against CDK6 (PDB ID: 6OQO)

In Silico ADME Analysis

The pharmacological properties of top-scored compounds were analyzed using the SwissADME server, presented in *Supplementary File 2.* Based on the Lipinski rule of five (LRF), the physicochemical features of the top 7 compounds in comparison to CCL were evaluated, illustrated in Table 3. These results showed that all compounds exhibited a molecular weight of ≤500 g/mol, except compound 57 (509.6 g/mol). All 7 compounds exhibited ≤ 10 rotatable bonds, indicating suitable oral bioavailability. Additionally, all compounds possessed ≤ 5 H-bond donors and ≤ 10 H-bond acceptors, also the total polar surface area (TPSA) of all compounds ranged < 140 A^2, indicating the drug-like properties of all compounds. Overall, all compounds followed LRF, suggesting their potential as a drug-like candidate, except for compound 57. Moreover, the fraction Csp3 for all compounds was also noted to be > 0.3 except for the compounds 34, 93, and 42. Therefore, all other compounds highlighted their increased risk of off-target interactions and poor solubility.

The lipophilicity of the compounds was measured as Log P across ILOGP, XLOGP, WLOGP, MLOGP, Silicos IT, and consensus LogP. The lipophilicity revealed that all compounds exhibited LogP < 5.00, indicating a balanced hydrophobicity of the compounds. Subsequently, the solubility was measured as log S across the following descriptors: ESOL-Log S, Ali Log S, and Silicos-IT Log S. The results showed that compound 21 showed the most promising solubility compared to all other compounds, indicating better oral bioavailability and easy formulation.

With the exception of compound 57, which exhibited poor blood-brain barrier (BBB) permeability, all compounds demonstrated significant gastrointestinal (GI) permeability and the capacity to penetrate the BBB. Additionally, the drug-likeness of the compounds was assessed using a range of criteria developed by Lipinski, Ghose, Veber, and Egan. All compounds, except compound 57, met the predefined criteria according to the drug-likeness results, suggesting that they could be effective treatment choices. The bioavailability of all drugs was moderate (0.55).

The medicinal chemistry of all compounds was investigated, and the findings showed that none of them had any structural anomalies, as shown by the lack of Brenk warnings or Pan Assay Interference (PAINS). Subsequently, the synthetic accessibility of compounds was also observed, which was measured on a scale of 1 to 10. The results suggested that compound 21 showed easy synthetic accessibility compared to others due to the range closer to 1, whereas the CCL exhibited the highest synthetic accessibility score of 4.90 among others, showing moderate ease of synthesis. The pharmacological profile suggested compound 21 as the most potent candidate for therapeutic purposes to combat GBM.

Table 3: Pharmacological assessment of top-scored compounds, assessed through the SwissADME server.

Codes	CCL	21	69	34	57	93	54	42

MW (g/mol) ≤ 500g/mol	462.57	362.47	399.49	418.49	509.6	419.91	415.49	385.46
Fraction Csp3	0.52	0.38	0.3	0.15	0.31	0.27	0.3	0.27
Rotatable bonds ≤10	5	5	4	4	7	5	6	5
H-bond acceptors ≤10	6	4	4	4	6	4	5	4
H-bond donors ≤5	1	1	1	1	2	1	1	1
TPSA (A^2) ≤140	75	58.87	73.45	68.52	97.2	73.45	82.68	73.45
iLOGP	3.64	3.53	3.08	3.1	3.82	2.85	3.33	2.68
XLOGP3	3.01	2.92	0.75	4.52	3.53	3.91	3.25	3.28
WLOGP	3.71	3.42	3.66	4.86	3.37	4.18	3.54	3.53
MLOGP	2.59	2.28	2.95	2.94	2.22	2.81	2.02	2.33
Silicos-IT Log P	2.69	3.17	3.6	4.58	3.66	3.59	3.01	2.95
Consensus Log P < 5.00	3.13	3.06	3.41	4	3.32	3.47	3.03	2.95
ESOL Log S	-4.64	-4.06	-4.96	-5.64	-5.21	-5.12	-4.59	-4.53
Ali Log S	-4.25	-3.82	-4.99	-5.68	-5.26	-5.15	-4.66	-4.5
Silicos-IT LogS	-6.90	-6.95	-7.71	-9.82	-8.86	-7.94	-7.45	-7.35
GIA	High	High	High	High	High	High	High	High
BBB permeability	Yes	Yes	Yes	Yes	No	Yes	No	Yes
Lipinski violations	0	0	0	0	1	0	0	0
Ghose violations	1	0	0	0	2	0	0	0
Veber violations	0	0	0	0	0	0	0	0
Egan violation	0	0	0	0	0	0	0	0
Bioavailability Score	0.55	0.55	0.55	0.55	0.55	0.55	0.55	0.55
PAINS alerts	0	0	0	0	0	0	0	0
Brenk alerts	0	0	0	0	0	0	0	0
Synthetic Accessibility	4.90	3.52	3.81	3.67	4.16	3.72	3.81	3.69

*MW=molecular weight, TPSA=total polar surface area, GIA=gastrointestinal absroption, BBB=blood-brain barrier, PAINS=pan-assay interference compounds.

Oral Bioavailability

The oral bioavailability of all top-screened compounds was assessed through SwissADME, across the following descriptors: size, polarity, flexibility, insaturation, insolubility, and lipophilicity (*Supplementary Figure 4*). The radar charts shown in Figure 6 indicate the normal physicochemical space for efficient oral bioavailability of the top 7 compounds, along with the R* drug. The radar charts portrayed that compounds CCL, 21, 69, 34, and 52 fell within the marked red zone of the chart, highlighting their potential for

ARTICLE IN PRESS

effective oral bioavailability. While compounds 57, 93, and 52 were marked outside the defined red zone, indicating their poor oral bioavailability.

Figure 6: Radar chart showing the normal physicochemical space for efficient oral bioavailability marked within the red space, evaluated through the SwissADME server.

Toxicity Assessment

The acute toxicity of the compounds are shown in *Supplementary Table 3*. The predicted toxicity results shown in Table 4 revealed that both CCL and compound 21 showed non-toxic behavior across all parameters except for acute oral toxicity, indicating immediate toxicity upon oral contact. Whereas, all other compounds also showed toxicity upon contact with the eyes, possessing eye irritation and corrosion. Notably, compound 42 was also predicted to show positive status for skin irritation and corrosion. These results indicated compound 21 as the least toxic compound amongst others.

Table 4: Toxicity prediction of seven top-scored compounds, predicted through StopTox.

Codes	Acute Inhalation Toxicity	Acute Oral Toxicity	Acute Dermal Toxicity	Eye Irritation and Corrosion	Skin Sensitization	Skin Irritation and Corrosion
CCL	Non-toxic	Toxic	Non-toxic	Non-toxic	Non-sensitizer	Negative
21	Non-toxic	Toxic	Non-toxic	Non-toxic	Non-sensitizer	Negative
69	Non-toxic	Toxic	Non-toxic	Toxic	Non-sensitizer	Negative
34	Non-toxic	Toxic	Non-toxic	Toxic	Non-sensitizer	Negative
57	Non-toxic	Toxic	Non-toxic	Toxic	Non-sensitizer	Negative
93	Non-toxic	Toxic	Non-toxic	Toxic	Non-sensitizer	Negative
54	Non-toxic	Toxic	Non-toxic	Toxic	Non-sensitizer	Negative
42	Non-toxic	Toxic	Non-toxic	Toxic	Non-sensitizer	Positive

DFT Studies

Based on the above *in silico* analysis, compound 21 was selected for density functional theory (DFT) studies using the Gaussian 09W program to gain valuable insights into the electronic and molecular properties of the lead compound, in comparison to the reference compound. The results, as illustrated in Table 5, show a comparative analysis of frontier molecular orbitals (FMOs) and global reactivity parameters between compound 21 and CCL.

The energy gap (ΔEGap) between the FMOs showed that compound 21 (4.21 eV) had a wider energy gap than CCL (3.44 eV), suggesting stronger chemical stability. In addition to having a slightly higher ionization potential (5.67 eV) than CCL (5.10 eV), compound 21 also had a lower electron affinity (1.46 eV) than CCL (1.66 eV), indicating that CCL was more likely to accept electrons. The electronegativity of compound 21 (6.57 eV) subsequently outperformed that of CCL (3.38 eV), indicating that compound 21 had a stronger propensity to draw electrons. Additionally, the softness and chemical hardness of both compounds were comparable, suggesting that their polarizability was balanced. In addition, compound 21 (3.02 eV) had a lower likelihood of receiving electrons than CCL (3.32 eV), according to the electrophilicity indices.

Table 5: Results of Koopmans' theorem-based DFT calculations of the global reactivity parameters of lead compound 21 and CCL.

Parameters for DFT analysis	Compound 21	CCL
HOMO **(a.u.)**	-0.20846	-0.18734
LUMO **(a.u.)**	-0.05361	-0.06095
Energy Gap (ΔE_{Gap}) **(eV)**	4.21	3.44
Ionization Potential (I) **(eV)**	5.67	5.10
Electron affinity (A) **(eV)**	1.46	1.66
Electronegativity χ **(eV)**	6.57	3.38
Electrochemical potential μ **(eV)**	-6.57	-3.38
Hardness η **(eV)**	2.11	1.72
Softness S **(eV^{-1})**	0.475	0.582
Electrophilicity ω **(eV)**	3.02	3.32

MESP surface mapping provides a thorough understanding of the electrophilic and nucleophilic areas of a compound. Compound 21 displayed more negative electrostatic potential areas, particularly around the carbonyl and hydroxyl groups, according to the MESP mapping in Figure 7. These areas are more likely to interact electrostatically and form advantageous hydrogen bonds when they contain positively charged active site residues such as lys43. In contrast, the red area indicates the propensity of compound 21 to take up electrons. The CCL MESP mapping, on the other hand, showed more noticeable red areas, suggesting a more polar nature and electron-receiving capacity. However, by indicating electron-rich areas, the blue region illustrates CCL's nucleophilic capability of CCL. Interestingly, the neutral surfaces of both compounds were emphasized by prominent green regions, indicating a moderate level of interaction potential.

Compound 21
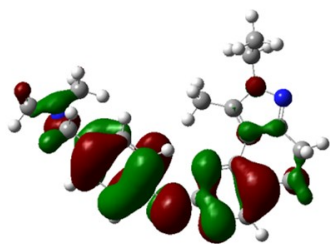
HOMO = -0.20846 a.u.
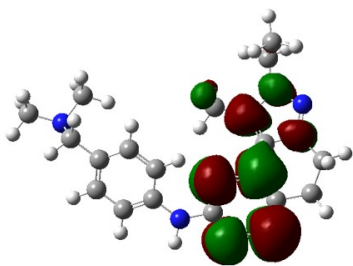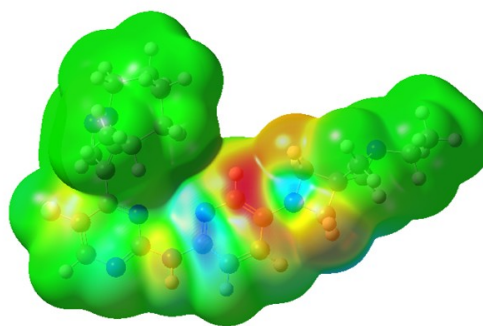
LUMO = -0.05361 a.u.
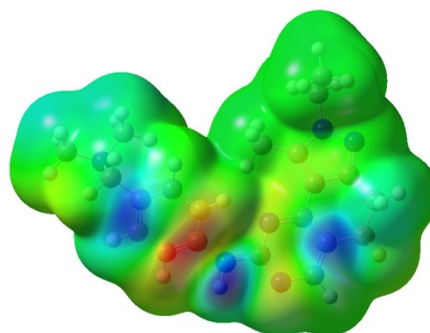
-7.494e-3   7.494e-3

CCL
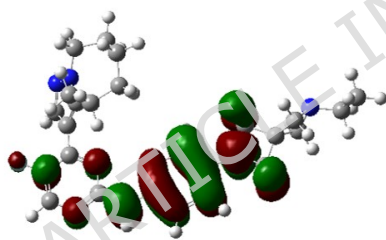
HOMO = -0.18734 a.u.
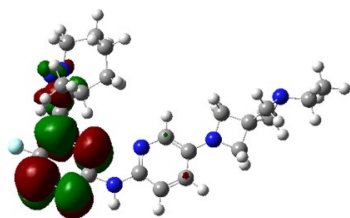
LUMO = -0.06095 a.u.

-8.313e-3   8.313e-3

Figure 7: Visual representation of frontier molecular orbitals (FMOs) and molecular electrostatic potential (MESP) surface mapping of compound 21 and CCL, visualized on gauss view 5.0.8 software.

MD Simulations

MD simulations were performed for 250 ns using Desmond (Schrödinger suite) to assess the structural stability and dynamic behavior of the CCL and compound 21 docked complexes under simulated physiological conditions (see Supplementary Figure 5). The plots in Figure 8 show the primary parameters, RMSD, RMSF, and Rg, which were utilized to evaluate the dynamic behavior of both complexes.

The structural stability of both complexes during the simulations was demonstrated by the RMSD charts. As demonstrated by the figure of compound 21, the RMSD of the protein backbone fluctuated up to 3.0Å, which stabilized after 50 ns. In contrast, the ligand RMSD fluctuated very little, ranging from 1.0 to 3.0 Å, suggesting that it was stable inside the CDK6 protein's active area. The ligand and protein backbone RMSD values, on the other hand, varied more dramatically, reaching 3.5 Å and 4.5 Å, respectively. The docked complex was more unstable and fluctuated more along the 250 ns trajectory, as indicated by the higher CCL RMSD value. According to the RMSD study, compound 21 exhibited a higher binding affinity for the target protein and a more stable and long-lasting association.

RMSF analysis was used to assess protein flexibility through 250 ns simulations. Specifically, the RMSF plots of compound 21 and CCL showed comparable fluctuation patterns in the protein loop region, with values ranging from 1.0–3.5 Å. Some peaks, especially those close to residues Agr168 to Leu176, which reached approximately 5 Å for compound 21 and 6 Å for CCL, revealed the receptor's flexible dynamic nature throughout the simulations. The compactness of the protein structure throughout the 250 ns simulations was briefly revealed by the Rg analysis of both substances. The

Rg value of the compound 21 complex remained between 19.6 Å and 20.4 Å over time, indicating a slow tendency toward the stability and compactness of the complex. The larger variance in Rg, which varied from 19.9 Å to 20.9 Å, suggests that the protein structure of CCL was less compact.
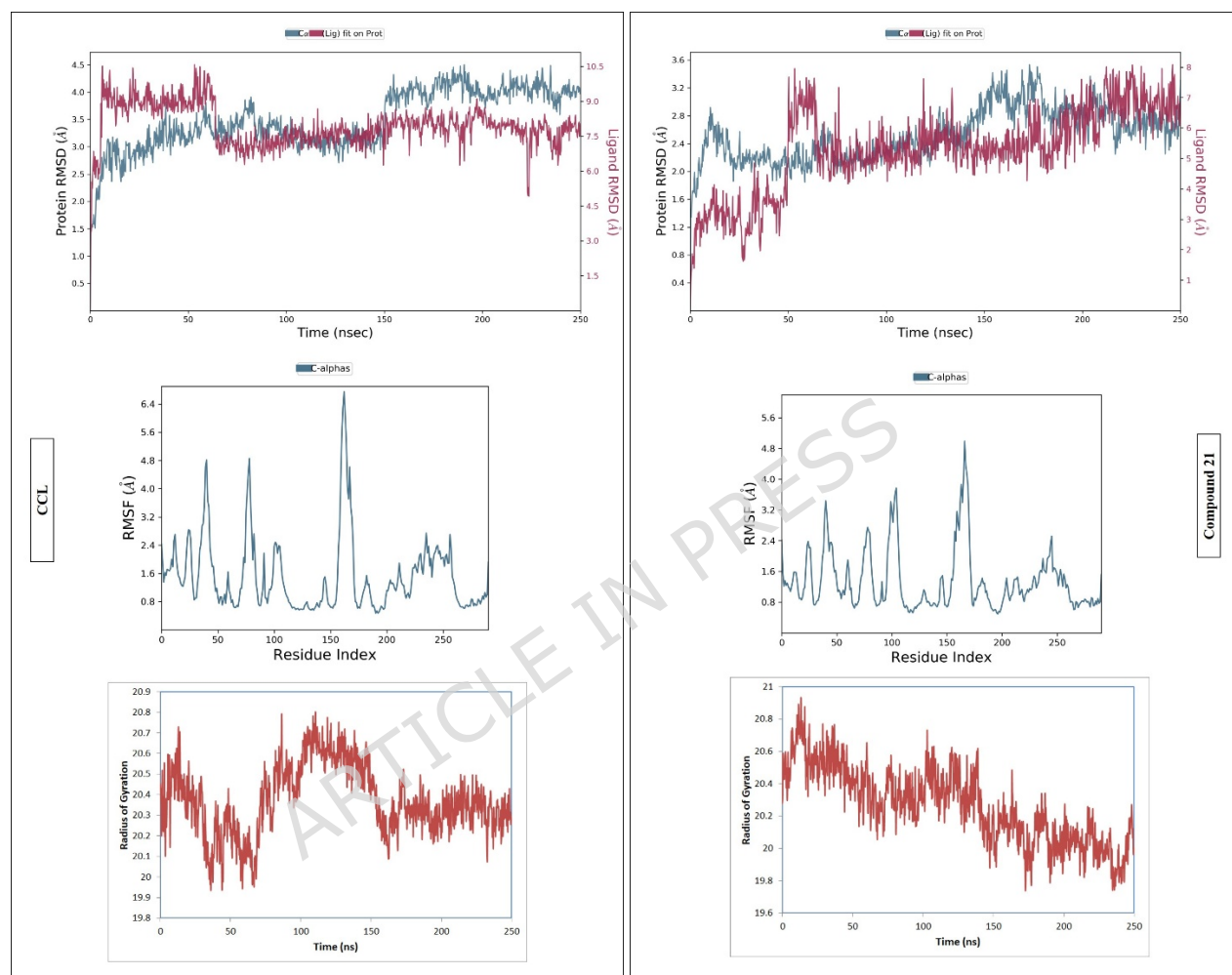

Figure 8: Graphical representation of root-mean square deviation (RMSD), root-mean square fluctuation (RMSF), and radius of gyration (Rg) of lead compound 21, in comparison to CCL.

Further information on the structural stability and interaction dynamics of CDK6 bound to compound 21 and CCL over the 250 ns simulations was obtained from the solvent-accessible surface area (SASA) and H-bond studies, as shown in Figure 9. According to the H-bond plot, both docked complexes had approximately 230–260 H-bonds across the 250 ns simulation period. The

compound 21 complex established enduring polar contacts with essential active site amino acid residues (Lys43 and His100) by preserving equilibrium and adhering to a regular H-bond pattern. The CCL complex showed more variations in the number of H-bonds, even though CCL produced enough of them to remain inside the CDK6 active site. These H-bond analyses demonstrated that 21 has a greater tendency to bind to CDK6.

Finally, SASA plot of compound 21 showed that it exhibited consistently lower and stabilized solvent exposure. The average SASA for compound 21 was maintained in a narrow range between ~140 to 150 $Å^2$, while CCL complex demonstrated higher fluctuation with more broad range ~140 to 158 $Å^2$. Hence, the SASA of compound 21 suggested its compact nature and efficient binding affinity with CDK6 protein, reinforcing its enhanced thermodynamic stability.
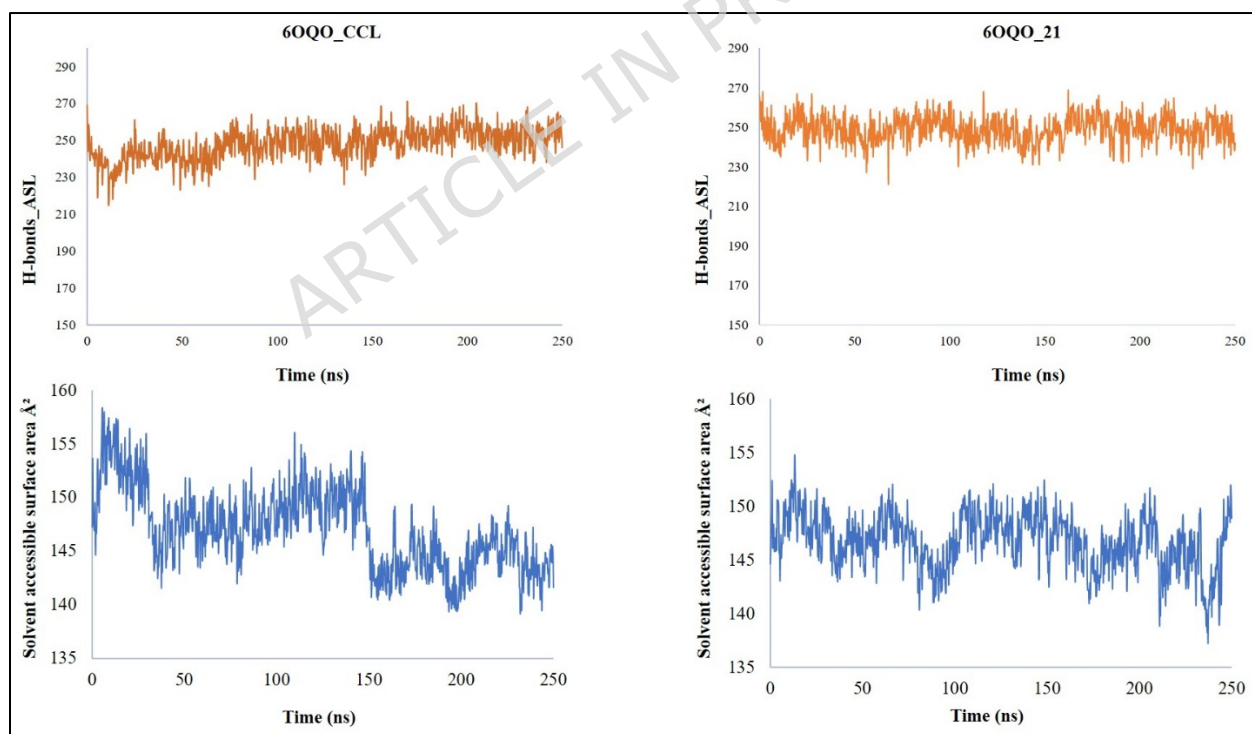

Figure 9: Graphical representation of hydrogen bond and solvent accessible surface area (SASA) analyses of lead compound 21, in comparison to CCL.

Protein-Ligand Contacts

Protein interactions with the ligand monitored throughout the simulation verified the docking results. As shown in Figure 9, these interactions are grouped by type and summarized. Hydrogen bonds, hydrophobic contacts, ionic interactions, and water bridges are the four types of protein-ligand interactions studied.

Crucially, the docking predictions matched the MD interaction profile of compound 21. Docking studies revealed that Lys43, His100, Val101, and Asp104 are important interacting residues through hydrogen bonding, π–π stacking, and hydrophobic interactions. These residues continued to interact with compound 21 during the MD simulation, indicating that the docking-predicted binding mode was mainly maintained under changing conditions.

The persistence of important contacts, especially with Asp104, Val101, His100, and hydrophobic residues such as Phe98 and Leu152, suggests a stable binding conformation throughout the 250 ns simulation, even though some interactions varied in strength over time, as expected in a dynamic solvated environment (Figure 10A).

Some of the interactions predicted during docking were retained in the protein–ligand contact diagram derived from the 250 ns MD simulation of the CCL–CDK6 complex. Asp102 and Asp104 exhibited frequent polar and hydrogen bonding interactions throughout the simulation, consistent with the docking results. Glu99 also made sporadic contributions to polar contacts, consistent with its involvement, as indicated by docking. During the MD trajectory, the polar residue His100, which generated hydrogen bonding connections during docking, showed fleeting contacts, suggesting decreased durability under dynamic conditions (Figure 10B).

CCL retained several key docking-predicted interactions during MD simulation, compound 21 demonstrated a higher persistence of critical polar and hydrophobic contacts, particularly with Asp104, Val101, His100, Lys43 and hydrophobic pocket residues.
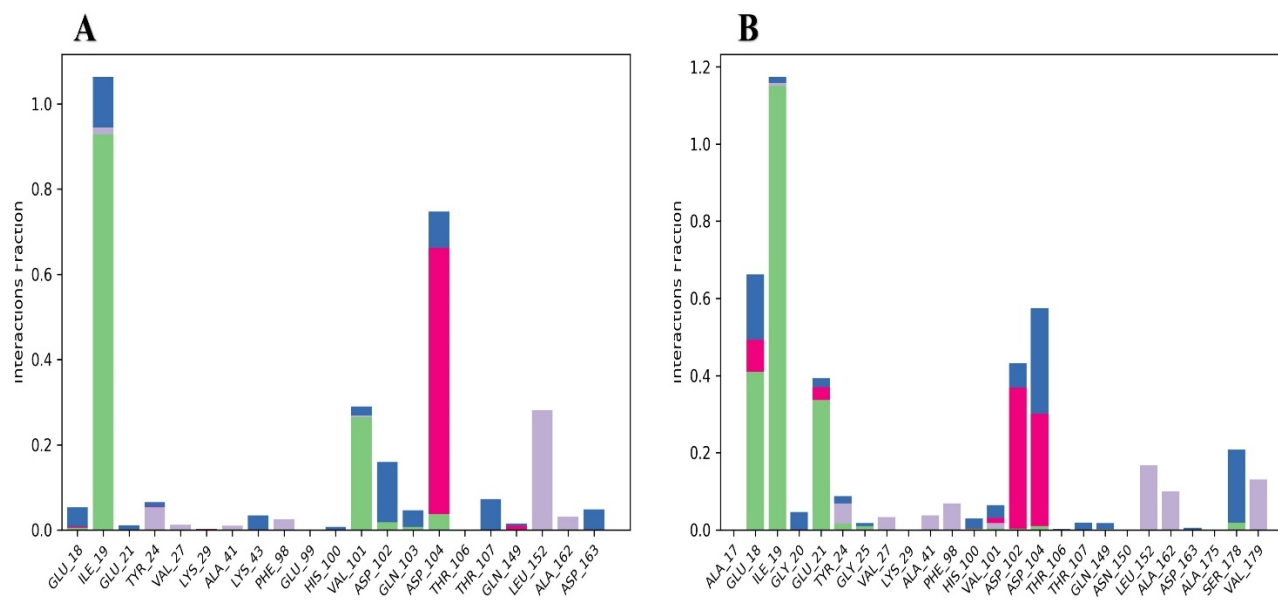
Figure 10. Protein-ligand contact histogram for compound 21 and CCL captured during 250ns of simulation

PCA Analysis

Principal Component Analysis (PCA) was performed on both compounds to identify the motion of docked complexes within simulations and assess the functionality and stability of the target protein over a 250-ns simulation trajectory. The PCA plots in Figure 11 for compound 21 show that the three primary components of the protein (PC1, PC2, and PC3) exhibited a restricted and stable conformation throughout the simulations. It is suggested that the protein structure was compact and its conformation stable during a trajectory of 250 ns because PC1 accounted for 31.17% of the entire motion, PC2 for 14.46%, and PC3 for 8.19% of (53.82%), respectively. In addition, the eigenvalue plot of compound 21 showed reduced variance, indicating that the compound 21 complex exhibited more consistent and dependable dynamic activity. Compared to the compound 21 complex, the PCA of the CCL complex revealed greater conformational changes and a wider motion, indicating weaker stability and less compactness. Compared to compound 21, the contributions of PC1, PC2, and PC3 to the total motion (66.255%) were more

dispersed and wide-ranging, accounting for 38.65, 17.73, and 9.87% of the total motion, respectively. This suggests that the target protein backbones exhibit a greater degree of variability. The eigenvalue plot showed that compound 21 was more stable on a real-time scale, and its eigenvalue was greater than that of the compound 21 complex.
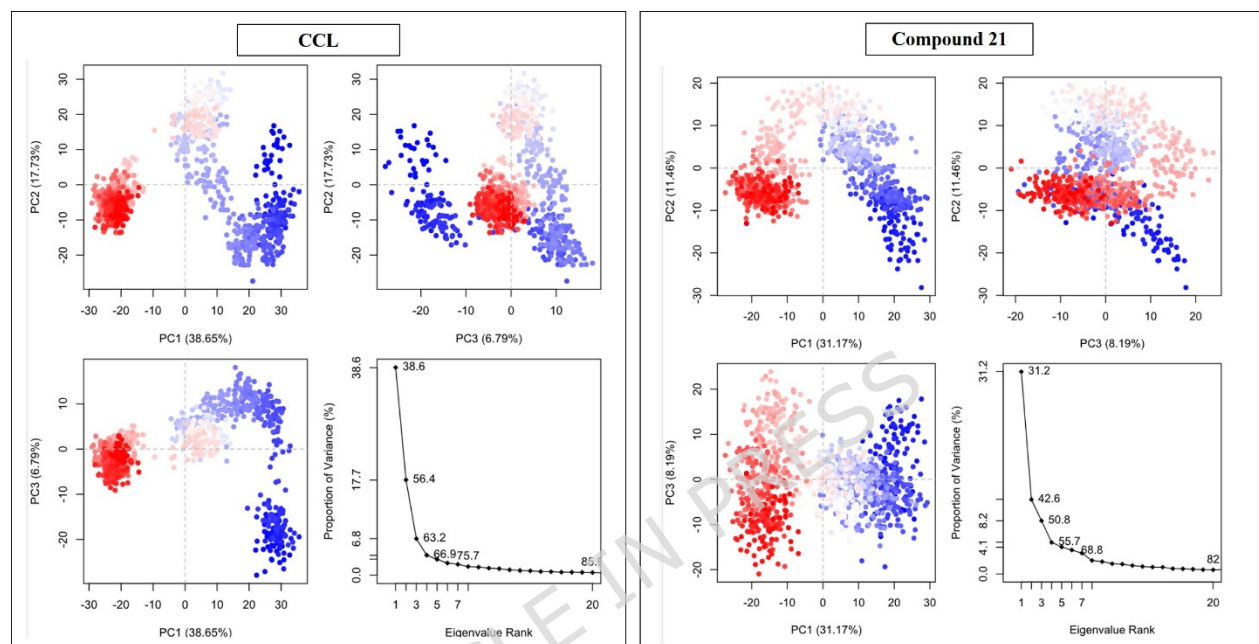

Figure 11: Graphical representation of principal components (PCs) for both lead compound 21 and CCL across PC1, PC2, and PC3.

DCCM Analysis

The overall dynamic behavior of residues within the target protein CDK6 was highlighted by dynamic cross-correlation matrix (DCCM) analysis, which displayed the correlated and anti-correlated mobility of residues along a 250 ns trajectory. Negative correlations showed residues moving in the opposite direction, whereas positive correlations showed residues moving in the same direction. For compound 21 (shown in cyan), the DCCM plots in Figure 12 show denser and more localized motion, indicating a stable dynamic network and a significant positive association among the residues. In contrast, the CCL complex showed weak and scattered correlations, indicating a less coordinated dynamic network with anti-correlated motion.
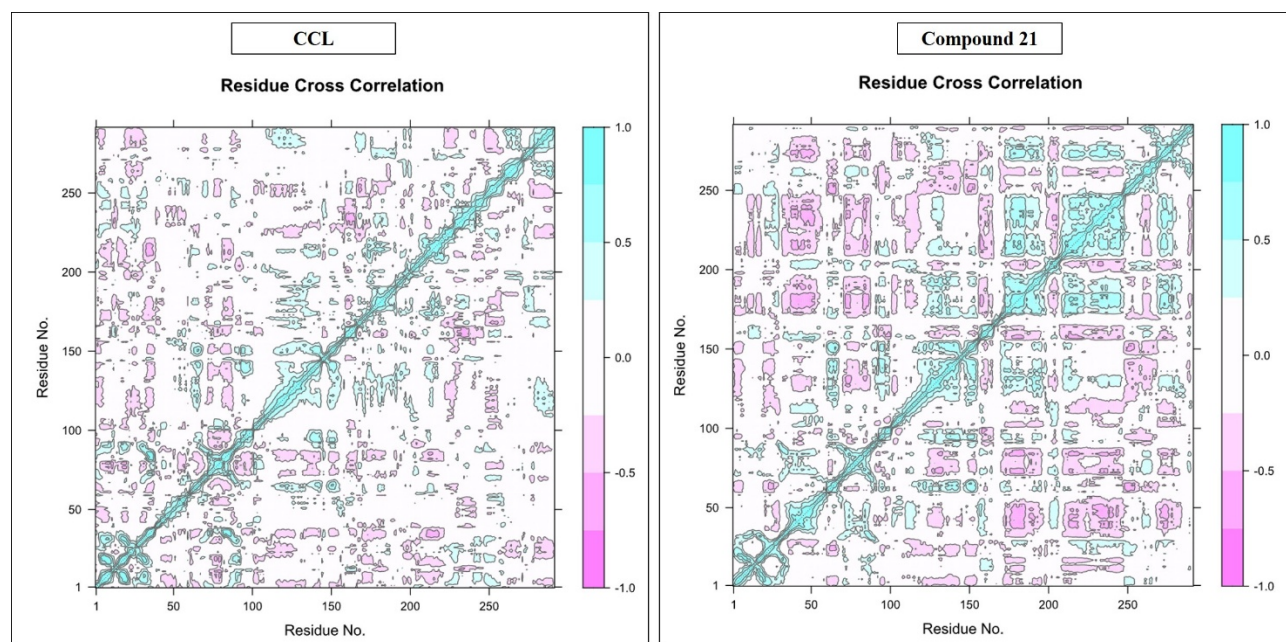
Figure 12: Graphical representation of dynamic cross-correlation matrix (DCCM) analysis of the lead compound 21 and CCL.

Molecular mechanics and generalized born surface area (MM-GBSA) calculations

The binding free energies obtained from the MMGBSA calculations are shown in Figure 13. The findings demonstrated that compound 21 had a much higher total binding free energy (Gbind) than CCL (-7.7748 kcal/mol), at -35.6127 kcal/mol. Both compounds displayed approximately equal energies in the dGbind lipophilic interactions, suggesting that their lipophilicity was balanced. The slightly higher energy (-24.6276 kcal/mol) was also demonstrated by the contribution of van der Waals interactions, suggesting that it had an appropriate binding affinity within the CDK6 receptor's active site (Supplementary Table 4). Furthermore, compared to compound 21, which had somewhat less severe electrostatic penalties, the CCL was significantly unfavorable, as indicated by the positive Coulomb energy. Due to the greater hydrophobic contacts, the H-bond contribution in both compounds remained low, and the dGbind packing of the compounds was zero, suggesting that there were very few steric collisions. Compound 21

exhibited a larger binding energy, lower electrostatic penalties, and considerable vdW interactions, which highlight its selectivity against CDK6, making it a strong contender overall, according to the MMGBSA data.
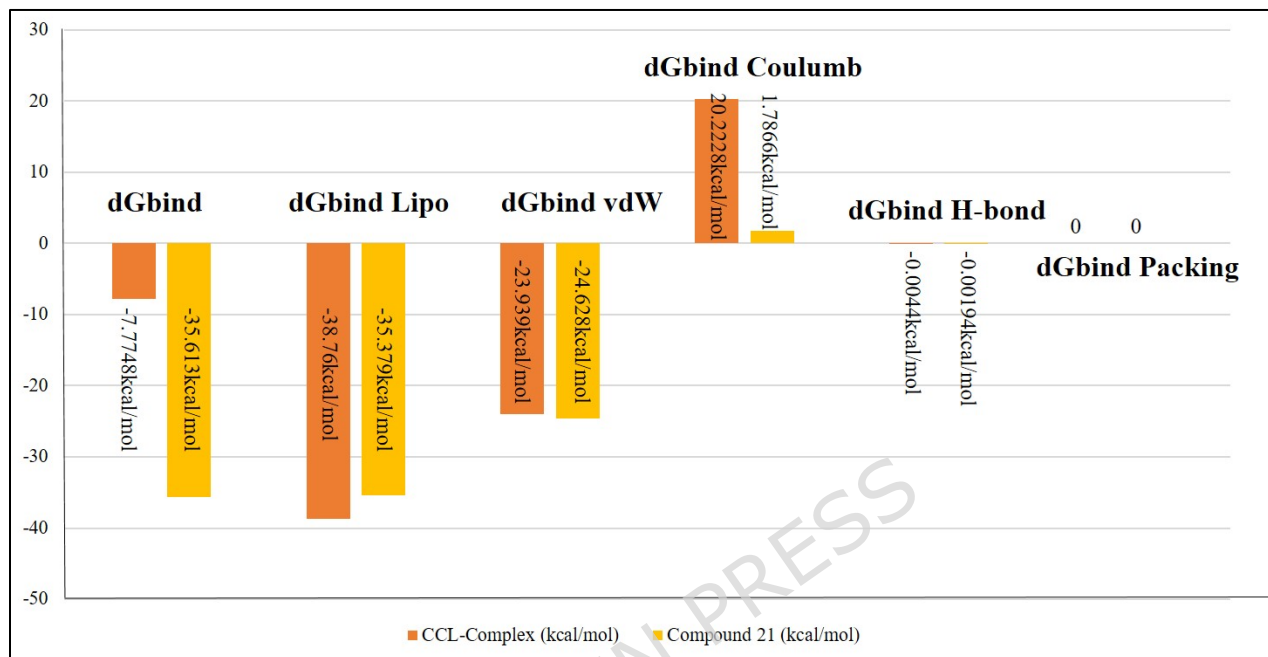

Figure 13: MMGBSA calculations of binding free energies of the lead compound 21 and CCL.

Discussion

GBM is characterized by abnormal proliferation and invasion of cancerous cells, ultimately leading to a poor prognosis. Conventional treatment strategies include surgical resection, chemotherapy, radiotherapy, and antiangiogenic therapies [51]. Currently, Temozolomide (TMZ) is considered the standard therapeutic agent for GBM [52], although post-therapeutic GBM recurrence and drug resistance have been observed in most cases, hence limiting the outcomes. Notably, recent studies have reported that CDK4/6 is often dysregulated in nearly 80% of all GBM cases [53], making it an attractive target for novel GBM therapeutic interventions. Therefore, the present study aimed to investigate the therapeutic potential of novel candidates by targeting CDK4/6 to overcome GBM recurrence and drug resistance.

In the modern era, the *in silico* approach is widely used in several studies to explore the therapeutic potential of small molecules in various diseases [44,54]. In this study, the novel small molecule inhibitors were screened through LBVS using the Swiss Similarity tool. The reference compound CCL (PDB ID: 6OQO) was chosen due to the presence of the primary amine group, particularly known to facilitate selective interactions, thereby limiting potential off-target effects [55]. The ChemBL library was screened, resulting in a total of 400 compounds, from which 109 were shortlisted based on a similarity threshold of 60%. This strategy was applied in a recent study, yielding 400 bioactive analogues. Additionally, the cluster pattern also demonstrated the presence of core scaffolds, which affirmed that LBVS retrieved a chemically diverse and non-redundant set of bioactive molecules. This underscores the probability of discovering a potential and selective candidate as a CDK6 inhibitor. The *in silico*-based tools were utilized, the analogues were analyzed, and the novel compound was proposed as a competent therapeutic agent to overcome drug resistance [56]. The short-listed 109 compounds were subjected to molecular docking to evaluate the binding affinity of novel compounds against the target receptor CDK6 (PDB ID: 6OQO) [39]. Previously, CDK6 (PDB ID: 6OQL) was studied, and the (R)-5-fluoro-4-(4-methyl-5,6,7,8-tetrahydro-4H-pyrazolo[1,5-a]azepin-3-yl)-N-(5-(4-methylpiperazin-1-yl)pyridin-2-yl)pyrimidin-2-amine was observed to have strong binding affinity; however, several structural modifications were performed, making it more selective against the CDK6 protein (PDB 6OQL) [39]. The results of docking against CDK6 (PDB ID: 6OQO) revealed significantly stronger binding affinity for all compounds. 48 compounds out of 109 compounds exhibited a docking score of more than CCL (-11.174 kcal/mol). These scores signified a better binding affinity of these novel compounds against the CDK6 protein. Additionally, the interaction analysis also showed the hotspot residues within the active site of CDK6 (PDB ID: 6OQO), which were crucial for understanding the interaction pattern and formulation of drug design. The key residues involved in interaction with

most of the compounds include Asp 102, Asp104, Glu99, His100, Lys43, Val101, Leu152, and Ala41, which contributed efficiently in forming both H-bond and hydrophobic interactions, generating a binding domain within the active site that facilitates the interactions. It was noteworthy that the involvement of His100 and Lys43 residues played a major role in making these compounds more selective and specific against CDK6 (PDB ID: 6OQO) to combat GBM, as it has been reported previously that the specificity and selectivity of CDK6 targets could be increased by the involvement of polar residues, particularly His100 and Lys43 [39]. The findings of the present study were aligned well with one of the previously reported computational analyses, revealing that His100, Val101, Asp102, and Asp104 were reported as vital amino acid residues for interaction [57].

The pharmacological and toxicological assessment is one of the crucial stages in drug development. Several studies have employed *in silico*-based tools to predict the ADME and toxicity of the compounds to observe their drug-like characteristics [58]. The present study underscored compound 21 as the most potent drug-like inhibitor in terms of both toxicity and ADME. The results of ADME presented in the present study adhere to LRF with an acceptable molecular weight (<500g/mol), ≤ 10 rotatable bonds, ≤ 10 H-bond acceptors, ≤ 5 H-bond donors, and TPSA ≤140 Å², all of which suggested a favorable oral bioavailability of these compounds [59]. Additionally, most of the compounds maintain a fraction Csp3 >0.3, highlighting an ideal saturation and minimized potential off-target activity. These results also aligned with the interaction pattern against CDK6, as the selectivity and specificity were also enhanced due to selective interaction with His100 and Lys43, hence reducing off-target effects. Furthermore, owing to its substantial gastrointestinal absorption and BBB permeability, compound 21 is a promising option for GBM inhibition. In the toxicity profile, compound 21 was also highlighted as non-toxic in vivo for inhalation, ocular irritation, cutaneous irritation, and skin sensitization. Despite the observation of oral

toxicity, it can be controlled using route-specific drug formulation techniques [60]. In general, the high solubility, safety profile, synthetic accessibility, and physicochemical stability of compound 21 lend credence to its potential as a lead molecule for CDK6 inhibition.

As lead compound 21 was determined to be the most appropriate CDK6 inhibitor based on the previously mentioned research, a DFT study was conducted for it. A molecule's global reactivity descriptors, specifically chemical hardness (η), softness (S), and the HOMO–LUMO energy gap, directly represent its chemical resistance and susceptibility. In general, molecules with a lower bandgap are softer and more reactive, while those with a wider energy gap are thought to be harder and more chemically stable [61]. Compound 21 demonstrated low softness (S = 0.475 eV^{-1}) and comparatively high chemical hardness (η = 2.11 eV) in the current study, suggesting a robust resistance to electronic deformation and decreased chemical reactivity. Compound 21 further supported its electrical stability by displaying a significant HOMO–LUMO energy gap (4.21 eV), which is consistent with these findings. The balanced reactivity and electrical stability of compound 21 are demonstrated by its greater energy gap (4.21 eV), which lowers the possibility of unexpected side effects and off-target interactions. This element is crucial for maintaining the stability of drug metabolism and medicine safety. The increased ionization potential (5.67 eV) of compound 21 also helped achieve appropriate pharmacokinetic stability by decreasing the possibility of metabolic deactivation. The electron affinity of compound 21 further supported its benign profile by showing that it was less successful in attracting potentially dangerous unwanted electrons. According to the interaction study, the increased electronegativity of compound 21 demonstrated its capacity to draw electrons and strengthen particular contacts with electron-rich CDK6 domains, such as Glu99 and His100. The DFT findings of the new chemical that was separated from LBVS aligned with a study that also showed the molecular properties of the LBVS compound

(ZINC000003015356) as a strong inhibitor of DPP4 [62]. The binding specificity of compound 21 was electronically justified by the DFT results, which also indicated moderate reactivity and good stability. These results were in accordance with the docking and interaction patterns.

The docking data showed that compound 21 (-122.811 kcal/mol) was more active than the reference compound CCL (-11.174 kcal/mol) against the CDK6 (PDB ID: 6OQO) receptor. MD simulations were performed to confirm these results. Many recent in silico investigations have employed this powerful computational technique to evaluate conformational stability, flexibility, and structural integrity. To assess the dynamic behavior of the CDK6 complex in real time, a 250 ns simulation was performed for lead compound 21 in the current investigation. According to the RMSD investigation, compound 21 stabilized with the receptor backbone in the first 50 ns, preserving equilibrium and allowing for a continuous fluctuation of up to 3.0 Å [63, 64]. However, ligand fluctuation remained within the range of 1.0–3.0 Å. The CCL and compound 21 complexes showed comparable fluctuation patterns in the RMSF analysis, with compound 21 displaying a range of aberrations limited to the CDK6 receptor's loop regions, which was considered acceptable. However, because RMSF value of CCL was higher than 6.0 Å, it demonstrated poor stability. Additionally, the PCA mentioned the compactness of the compound 21 complex, which was emphasized by the Rg analysis. Additionally, the compound 21 complex showed a strong positive correlation in the DCCM investigation, as it is indicating that the residues moved in unison in real-time [65]. Furthermore, the larger binding free energy indicated greater stability and possible inhibitory efficiency, according to the MMGBSA calculations [66]. As a result, during the 250 ns simulations, the dGbind energy (-35.6127 kcal/mol) matched the high binding affinity and stability. Consistent with the ADME results, the balanced lipophilicity of 21 also suggested that it may penetrate the blood-brain barrier, which is crucial for the treatment of GBM. Due in large part to the presence of the primary amine,

compound 21, which is necessary for advantageous interactions with His100 and Lys43, also showed very low instability. Because of its significant binding affinity, accurate interactions with essential residues required to target CDK6 in GBM with little fluctuation, and ideal compact structure of the docked complex, compound 21 was chosen by the simulation study as a viable CDK6 inhibitor.

The integrated in silico-based study concluded that compound 21 exhibited remarkable drug-like features, strong molecular and electronic stabilities, and stable dynamic behavior in real-time. It also exhibited the highest binding affinity and interacted with the critical residues of CDK6. Taken together, these findings show that compound 21 is a strong, dependable, and specific CDK6 inhibitor that can successfully treat GBM and overcome treatment resistance. Given the aforementioned possibility, the next phase of drug development may involve experimental validation and logical optimization. Both in vivo pharmacokinetic investigations and in vitro biochemical evaluation assays can be used to evaluate the anti-proliferative qualities in the GBM model. Furthermore, compound 21 can be optimized by conducting structure–activity relationship (SAR) investigations that focus on important residues, particularly Lys43 and His100. Simultaneously, formulation techniques for GBM treatment management and the off-target potential of compound 21 should be prioritized [60].

Conclusion

According to the findings of the present computational investigation, compound 21 is a selective and promising CDK6 inhibitor that can be used to treat GBM. In contrast to CCL, compound 21 showed an impressive binding affinity (-12.811 kcal/mol) to CDK6 (PDB ID: 6OQO), according to the docking study. Important bonds were also established by the chemical with important residues, including Lys43 and His100, which are mainly recognized for their selectivity in CDK6 inhibition. Furthermore, the toxicity profile and ADME of

compound 21 were also good. Further, DFT studies supported the electronic stability and reactivity of compound 21 with minimal off-target risks, while simulations validated the dynamic stability and acceptable conformational changes with flexibility within the docked complex. Together, these findings suggested compound 21 as a suitable candidate warranting future experimental validation through *in vitro* and *in vivo* analysis, paving the path for therapeutic management in GBM.

Declaration
Ethical statements
Not Applicable
Conflict of interest
The authors declare that there is no conflict of interest regarding the publication of this article.

Author contribution
MM and HM wrote the initial manuscript. IH, TAC constructed the figures and tables and finalized the manuscript. MUK and BSA conceptualized and supervised the project. All the authors reviewed and approved the final version of the manuscript.
Data Availability statement

The data generated from the study has been clearly presented in the results and supplementary material.

References

1.   Darlix, A. *et al.* Epidemiology for primary brain tumors: a nationwide population-based study. *J. Neurooncol.* **131**, 525–546 (2017).

2.   Tykocki, T. & Eltayeb, M. Ten-year survival in glioblastoma. A systematic review. *J. Clin. Neurosci. Off. J. Neurosurg. Soc. Australas.* **54**, 7–13 (2018).

3.   Pouyan, A. *et al.* Role of lncRNAs in brain tumors. *Gene reports* 101904 (2024).

4.   Ostrom, Q. T. *et al.* CBTRUS Statistical Report: Primary Brain and Other Central Nervous System Tumors Diagnosed in the United States in 2015-2019. *Neuro. Oncol.* **24**, v1–v95 (2022).

5.   Tan, A. C. *et al.* Management of glioblastoma: State of the art and future directions. *CA. Cancer J. Clin.* **70**, 299–312 (2020).

6.   Grochans, S. *et al.* Epidemiology of Glioblastoma Multiforme-Literature Review. *Cancers (Basel).* **14**, (2022).

7.   Khabibov, M. *et al.* Signaling pathways and therapeutic approaches in glioblastoma multiforme (Review). *Int. J. Oncol.* **60**, (2022).

8.   Tamimi, A. F. & Juweid, M. Epidemiology and outcome of glioblastoma. *Exon Publ.* 143–153 (2017).

9.   Lubanska, D. & Porter, L. Revisiting CDK Inhibitors for Treatment of Glioblastoma Multiforme. *Drugs R. D.* **17**, 255–263 (2017).

10.   Bury, M., Le Calvé, B., Ferbeyre, G., Blank, V. & Lessard, F. New Insights into CDK Regulators: Novel Opportunities for Cancer Therapy. *Trends Cell Biol.* **31**, 331–344 (2021).

11.   Brennan, C. W. *et al.* The somatic genomic landscape of glioblastoma. *Cell* **155**, 462–477 (2013).

12.   Molinaro, A. M., Taylor, J. W., Wiencke, J. K. & Wrensch, M. R. Genetic and molecular epidemiology of adult diffuse glioma. *Nat. Rev. Neurol.* **15**, 405–417 (2019).

13.   Olmez, I. *et al.* Combined CDK4/6 and mTOR inhibition is synergistic against glioblastoma via multiple mechanisms. *Clin. Cancer Res.* **23**, 6958–6968 (2017).

14.   Malumbres, M. & Barbacid, M. To cycle or not to cycle: a critical decision in cancer. *Nat. Rev. cancer* **1**, 222–231 (2001).

15.   Sherr, C. J., Beach, D. & Shapiro, G. I. Targeting CDK4 and CDK6: From Discovery to Therapy. *Cancer Discov.* **6**, 353–367 (2016).

16.   Patnaik, A. *et al.* Efficacy and Safety of Abemaciclib, an Inhibitor of CDK4 and CDK6, for Patients with Breast Cancer, Non-Small Cell Lung Cancer, and Other Solid Tumors. *Cancer Discov.* **6**, 740–753 (2016).

17.   Schettini, F. *et al.* CDK 4/6 Inhibitors as Single Agent in Advanced Solid Tumors. *Front. Oncol.* **8**, 608 (2018).

18.   Taylor, J. W. *et al.* Phase-2 trial of palbociclib in adult patients with recurrent RB1-positive glioblastoma. *J. Neurooncol.* **140**, 477–483 (2018).

19.   Raub, T. J. *et al.* Brain Exposure of Two Selective Dual CDK4 and CDK6 Inhibitors and the Antitumor Activity of CDK4 and CDK6 Inhibition in Combination with Temozolomide in an Intracranial Glioblastoma Xenograft. *Drug Metab. Dispos.* **43**, 1360–1371 (2015).

20.   Goel, S., Bergholz, J. S. & Zhao, J. J. Targeting CDK4 and CDK6 in cancer. *Nat. Rev. Cancer* **22**, 356–372 (2022).

21.   Kim, H. *et al.* Integrative genome analysis reveals an oncomir/oncogene cluster regulating glioblastoma survivorship. *Proc. Natl. Acad. Sci. U. S. A.* **107**, 2183–2188 (2010).

22.   Deng, X. *et al.* miR-124 radiosensitizes human glioma cells by targeting

CDK4. *J. Neurooncol.* **114**, 263–274 (2013).

23. López, G. Y. *et al.* The genetic landscape of gliomas arising after therapeutic radiation. *Acta Neuropathol.* **137**, 139–150 (2019).

24. Dai, Z. *et al.* Oxymatrine induces cell cycle arrest and apoptosis and suppresses the invasion of human glioblastoma cells through the EGFR/PI3K/Akt/mTOR signaling pathway and STAT3. *Oncol. Rep.* **40**, 867–876 (2018).

25. Michaud, K. *et al.* Pharmacologic inhibition of cyclin-dependent kinases 4 and 6 arrests the growth of glioblastoma multiforme intracranial xenografts. *Cancer Res.* **70**, 3228–3238 (2010).

26. Wen, P. *et al.* CTNI-12. Preliminary results of the abemaciclib arm in the individualized screening trial of innovative glioblastoma therapy (INSIGHT): a phase II platform trial using Bayesian adaptive randomization. *Neuro. Oncol.* **22**, ii44–ii44 (2020).

27. Pombo Antunes, A. R. *et al.* Understanding the glioblastoma immune microenvironment as basis for the development of new immunotherapeutic strategies. *Elife* **9**, e52176 (2020).

28. Li, H. *et al.* Design, synthesis, and biological characterization of a potent STAT3 degrader for the treatment of gastric cancer. *Front. Pharmacol.* **13**, 944455 (2022).

29. Lieblein, J. C. *et al.* STAT3 can be activated through paracrine signaling in breast epithelial cells. *BMC Cancer* **8**, 302 (2008).

30. Brighi, N. *et al.* Prospective Evaluation of MGMT-Promoter Methylation Status and Correlations with Outcomes to Temozolomide-Based Chemotherapy in Well-Differentiated Neuroendocrine Tumors. *Curr. Oncol.* **30**, 1381–1394 (2023).

31. Mir, T., Pond, G. & Greenspoon, J. N. Outcomes in Elderly Patients with Glioblastoma Multiforme Treated with Short-Course Radiation Alone Compared to Short-Course Radiation and Concurrent and Adjuvant Temozolomide Based on Performance Status and Extent of Resection. *Curr. Oncol.* **28**, 2399–2408 (2021).

32. Chen, Y.-F. *et al.* TP3, an antimicrobial peptide, inhibits infiltration and motility of glioblastoma cells via modulating the tumor microenvironment. *Cancer Med.* **9**, 3918–3931 (2020).

33. Pan, L., Chen, X., Rassool, F. V., Li, C. & Lin, J. LLL12B, a Novel Small-Molecule STAT3 Inhibitor, Induces Apoptosis and Suppresses Cell Migration and Tumor Growth in Triple-Negative Breast Cancer Cells. *Biomedicines* **10**, (2022).

34. Jalili-Nik, M. *et al.* Zerumbone Promotes Cytotoxicity in Human Malignant Glioblastoma Cells through Reactive Oxygen Species (ROS) Generation. *Oxid. Med. Cell. Longev.* **2020**, 3237983 (2020).

35. Miao, Y. *et al.* Anti-cancer effect of targeting fibroblast activation protein

alpha in glioblastoma through remodeling macrophage phenotype and suppressing tumor progression. *CNS Neurosci. Ther.* **29**, 878–892 (2023).

36. Omoruyi, S. I., Ekpo, O. E., Semenya, D. M., Jardine, A. & Prince, S. Exploitation of a novel phenothiazine derivative for its anti-cancer activities in malignant glioblastoma. *Apoptosis* **25**, 261–274 (2020).

37. Turner, N. C. *et al.* Overall survival with palbociclib and fulvestrant in advanced breast cancer. *N. Engl. J. Med.* **379**, 1926–1936 (2018).

38. Xiao, J. *et al.* CDK4/6 inhibition enhances oncolytic virus efficacy by potentiating tumor-selective cell killing and T-cell activation in refractory glioblastoma. *Cancer Res.* **82**, 3359–3374 (2022).

39. Bronner, S. M. *et al.* Design of a brain-penetrant CDK4/6 inhibitor for glioblastoma. *Bioorg. Med. Chem. Lett.* **29**, 2294–2301 (2019).

40. Backman, T. W. H., Cao, Y. & Girke, T. ChemMine tools: an online service for analyzing and clustering small molecules. *Nucleic Acids Res.* **39**, W486-91 (2011).

41. Mishra, A., Mulpuru, V. & Mishra, N. An Interaction Network Driven Approach for Identifying Cervical, Endometrial, Vulvar Carcinomic Biomarkers and Their Multi-targeted Inhibitory Agents from Few Widely Available Medicinal Plants. *Appl. Biochem. Biotechnol.* **195**, 6893–6912 (2023).

42. Akbar, S., Das, S., Iqubal, A. & Ahmed, B. Synthesis, biological evaluation and molecular dynamics studies of oxadiazine derivatives as potential anti-hepatotoxic agents. *J. Biomol. Struct. Dyn.* **40**, 9974–9991 (2022).

43. Seeliger, D. & de Groot, B. L. Conformational transitions upon ligand binding: holo-structure prediction from apo conformations. *PLoS Comput. Biol.* **6**, e1000634 (2010).

44. Rauf, A. *et al.* Aldose reductase inhibitory evaluation and in silico studies of bioactive secondary metabolites isolated from Fernandoa. adenophylla (Wall. ex G. Don). *J. Mol. Struct.* 141308 (2025).

45. Singh, J., Deng, Z., Narale, G. & Chuaqui, C. Structural interaction fingerprints: a new approach to organizing, mining, analyzing, and designing protein-small molecule complexes. *Chem. Biol. Drug Des.* **67**, 5–12 (2006).

46. Daina, A., Michielin, O. & Zoete, V. SwissADME: a free web tool to evaluate pharmacokinetics, drug-likeness and medicinal chemistry friendliness of small molecules. *Sci. Rep.* **7**, 42717 (2017).

47. Borba, J. V. B. *et al.* STopTox: An in Silico Alternative to Animal Testing for Acute Systemic and Topical Toxicity. *Environ. Health Perspect.* **130**, 27012 (2022).

48. Raczyńska, E. D. *et al.* Nitriles with high gas-phase basicity—Part II Transmission of the push–pull effect through methylenecyclopropene and cyclopropenimine scaffolds intercalated between different electron donor (s) and the cyano N-protonation site. *Molecules* **27**, 4370 (2022).

49. Tsuneda, T., Song, J.-W., Suzuki, S. & Hirao, K. On Koopmans' theorem in density functional theory. *J. Chem. Phys.* **133**, 174101 (2010).

50. Pouyan, A. *et al.* Glioblastoma multiforme: insights into pathogenesis, key signaling pathways, and therapeutic strategies. *Mol. Cancer* **24**, 58 (2025).

51. Onciul, R. *et al.* Deciphering glioblastoma: fundamental and novel insights into the biology and therapeutic strategies of gliomas. *Curr. Issues Mol. Biol.* **46**, 2402–2443 (2024).

52. Ghaznavi, H. *et al.* New insights into targeted therapy of glioblastoma using smart nanoparticles. *Cancer Cell Int.* **24**, 160 (2024).

53. Freitag, T. *et al.* Combined inhibition of EZH2 and CDK4/6 perturbs endoplasmic reticulum-mitochondrial homeostasis and increases antitumor activity against glioblastoma. *NPJ Precis. Oncol.* **8**, 156 (2024).

54. Akram, A. *et al.* Silibinins and curcumin as promising ligands against mutant cystic fibrosis transmembrane regulator protein. *AMB Express* **14**, 84 (2024).

55. Abdelkarim, H. *et al.* Design, Synthesis, Molecular Modeling, and Biological Evaluation of Novel Amine-based Histone Deacetylase Inhibitors. *ChemMedChem* **12**, 2030–2043 (2017).

56. Alanazi, A. *et al.* A combined in silico and MD simulation approach to discover novel LpxC inhibitors targeting multiple drug resistant Pseudomonas aeruginosa. *Sci. Rep.* **15**, 1–19 (2025).

57. Khan, M. *et al.* Computational exploration of allosteric inhibitors targeting CDK4/CDK6 proteins: a promising approach for multi-target drug development. *J. Biomol. Struct. Dyn.* **43**, 3783–3801 (2025).

58. Rauf, A. *et al.* Anticancer potential of flavonoids isolated from Pistacia chinensis against glioblastoma (U87) cell line: Extensive in vitro and in silico research. *Eurasian J. Med. Oncol.* 5768 (2025).

59. Lipinski, C. A., Lombardo, F., Dominy, B. W. & Feeney, P. J. Experimental and computational approaches to estimate solubility and permeability in drug discovery and development settings. *Adv. Drug Deliv. Rev.* **46**, 3–26 (2001).

60. Chou, W.-C. *et al.* Development of a multi-route physiologically based pharmacokinetic (PBPK) model for nanomaterials: a comparison between a traditional versus a new route-specific approach using gold nanoparticles in rats. *Part. Fibre Toxicol.* **19**, 47 (2022).

61. Guendouzi, A., et al., *Unveiling Novel Hybrids Quinazoline/Phenylsulfonylfuroxan Derivatives with Potent Multi-Anticancer Inhibition: DFT and In Silico Approach Combining 2D-QSAR, Molecular Docking, Dynamics Simulations, and ADMET Properties.* ChemistrySelect, 2024. **9**(43): p. e202404283.

62. Zare, F. *et al.* A combination of virtual screening, molecular dynamics simulation, MM/PBSA, ADMET, and DFT calculations to identify a potential DPP4 inhibitor. *Sci. Rep.* **14**, 7749 (2024).

63. Mishra, S. K. *et al.* Unveiling the molecular activity of HIV towards the CD4: A study based on subtype C via docking and dynamics approach. *J. Genet. Eng. Biotechnol.* **23**, 100457 (2025).

64. Manzoor, H., et al., *Computational identification and evaluation of novel PD-L1 inhibitors for cancer immunotherapy.* Scientific Reports, 2025. **15**(1): p. 33787

65. Manzoor, H., et al., *Citronellol silver nanoconjugates as a therapeutic strategy for glioblastoma through computational and experimental evaluation.* Sci Rep, 2025. **15**(1): p. 34076.

66. Manzoor, H., et al., *Linalool-based silver nanoconjugates as potential therapeutics for glioblastoma: in silico and in vitro insights.* PLOS ONE, 2025. **20**(6): p. e0325281